The use of microsphere assistance in interference microscopy with high numerical aperture objective lenses

Lucie Hüser[a], Tobias Pahl[a], Marco Künne[a], and Peter Lehmann[a]

[a]University of Kassel, EECS, Measurement Technology Group
Wilhelmshöher Allee 71, 34121 Kassel, Germany

ABSTRACT

Various attempts have been discussed to overcome the lateral resolution limit and thus to enlarge the fields of application of optical interference microscopy. Microsphere assisted microscopy and interferometry have proven that the imaging of structures well below Abbe's resolution limit through near-field assistance is possible if microspheres are placed on the measured surface and utilized as near-field assisting imaging elements. The enhancement of the numerical aperture by the microspheres as well as photonic nanojets were identified to explain the resolution enhancement, but also whispering gallery modes and evanescent waves are assumed to have an influence. Up to now, to the best of our knowledge there is no complete understanding of the underlying mechanisms and no model enabling to examine ideal imaging parameters. This contribution is intended to clarify, how much the lateral resolution of an already highly resolving Linnik interferometer equipped with 100x, NA 0.9 objective lenses can be further improved by microspheres. Our simulation model is based on rigorous near-field calculations combined with the diffraction limited illumination and imaging process in an interference microscope. Here, we extend the model with respect to microsphere assisted interference microscopy providing a rigorous simulation of the scattered electric field directly above the sphere. Simulation and experimental results will be compared in the 3D spatial frequency domain and discussed in context with ray-tracing computations in order to achieve an in-depth understanding of the underlying mechanism of resolution enhancement by the mircosphere.

Keywords: Interference microscopy, microsphere assistance, resolution enhancement

1. INTRODUCTION

Due to the ongoing trend towards miniaturization high-resolution optical imaging and 3D microscopy is highly relevant in certain fields of science and technology. This is particularly true for interference microscopy, one of the most established techniques for micro- and nano-structure measurement. As the lateral resolution $\Lambda_{\min}$ follows the Abbe criterion

$$\Lambda_{\min} = \frac{\lambda}{2\,\mathrm{NA}}, \tag{1}$$

the conventional way of improving the lateral resolution capabilities of microscopes is to increase the numerical aperture $\mathrm{NA} = n \sin\theta_{\max}$ of the objective lenses and to reduce the wavelength λ of light. For air as the surrounding medium with the refractive index $n = 1$ the numerical aperture solely depends on the maximum angle $\theta_{\max}$, which is the maximum angle of incidence with respect to the optical axis and the maximum scattering or reflection angle that is captured by the microscope objective lens. In recent years microsphere assistance has been proposed in order to improve the lateral resolution capabilities of conventional optical brightfield microscopes.[1]

A similar approach demonstrates what is called the super-resolving behavior of liquid-immersed microspheres[2] and points out the advantages compared to other resolution enhancement techniques.[3] Microsphere assistance was also successfully applied in context with confocal microscopy.[4] In addition, the illumination conditions with microsphere support and dark field microscopy were examined.[5,6]

Further author information: (Send correspondence to Lucie Hüser)
L. H.: E-mail: lucie.hueser@uni-kassel.de, Phone: +49 561 804-6505
P. L.: E-mail: p.lehmann@uni-kassel.de, Phone: +49 561 804-6313

More recently, microsphere assistance was also applied in white light interference microscopy.[7] For phase-shifting interferometry it was shown that with the support of microspheres applied in the near-field it is possible to extend the resolution limit for interferometric height profile measurements.[8,9] Numerical apertures in the range of 0.3 to 0.85 were used, enabling access to high-frequency image information through the improvement of the optical resolution. Thus, high-spatial-frequency surface height information could be obtained by white-light and phase-shifting interferometers in both, Linnik as well as Mirau configurations.[10–12]

To explain the effect of the resolution enhancement, photonic nanojets are often referred to.[13–15] These describe the focus of light on the backside of a microsphere illuminated with a plane wave from the top. On the scale of microspheres, this focus is characterized by its high intensity and narrow waist.[16] Numerous papers have been published, studying the behavior and engineering of photonic nanojets.[17,18] Also the role of evanescent waves and whispering gallery modes has been considered.[19,20] For further details it is referred to a recent review paper that gives an detailed overview of the state-of-the-art in microsphere-assisted microscopy.[21] Since incoherent Koehler illumination is applied in conventional brightfield and in interference microscopy the microspheres are illuminated by multiple plane waves incident under various angles. Annular illumination of the outer region of microspheres turned out to affect the achieved resolution enhancement.[22,23] Nevertheless, till now there is no complete and widely accepted explanation of the resolution enhancement by microspheres in conventional microscopy and interferometry. For this reason, further analysis of the underlying physical principles is of predominant interest. Analyzing interference microscopes in the three-dimensional (3D) spatial frequency domain by use of the 3D transfer function (TF) of the imaging system gives physical insight into the relevant transfer characteristics. Sheppard et al.[24] introduced a model which represents the imaging process of confocal microscopes in the 3D spatial frequency domain. This model was applied in further publications to surface profile reconstruction in confocal microscopy[25,26] and later introduced as the foil model in coherence scanning interferometry.[27,28] We recently extended this model by treating the reference mirror in the same way as the object's surface[29] and pointed out the analogy with the 3D TF of a brightfield reflection microscope.[30] We further recognized that the transfer characteristics of 3D microscopes strongly depend on the scattering characteristics of the surface (single point scatterers, mirror-like surfaces or diffraction gratings) and the spectral characteristics of the light source.[31]

Analyzing the interferometric measurement data in the 3D spatial frequency domain, the influence of microspheres on the transfer behavior of the optical system could already be shown.[23,32] In the following, the transfer characteristics of a high-resolution Linnik interferometer with and without microsphere assistance is pointed out by 3D spatial frequency domain analysis of 3D image stacks of periodic grating structures. Comparison of the results exhibits that the transfer characteristics of microspheres described in the 3D frequency domain are closely related to the angular ranges of incident, reflected and diffracted light rays. Thus, ray-tracing computations of light propagation through and inside the microsphere give further insight. Finally, experimental results obtained from gratings of different periods are compared to results of simulations based on rigorous FEM computations.

2. EXPERIMENTAL SETUP

The Linnik interferometer scetched in Fig. 1a and displayed in Fig. 1c is used to record interference images at certain height positions during a depth scan. This results in the so-called 3D image stack. Since our intention is to compare the resolution enhancement introduced by a microsphere in an already highly resolving microscope, we use two high-resolution microscope objective lenses (MO) with 100x magnification and an NA of 0.9, which still provide a working distance of 1 mm. A scientific CMOS camera records the image stack. For illumination a royalblue LED emitting at a center wavelength of $\lambda = 440\,\mathrm{nm}$ arranged in a Köhler illumination setup and a TM polarizer are utilized.

The depth scan is carried out using a precision piezo stage moving the object under investigation axially. Small height steps of typically 20 nm between two consecutive image frames are chosen in order to obtain a high number of sample points, which allows low-pass filtering to further reduce signal noise. The resulting image stack is analyzed pixel by pixel using envelope and phase evaluation algorithms in order to reconstruct the 3D topography of the surface.[33]

When placing microspheres on the surface to be measured, these spheres are put on the object's surface in a liquid emulsion for practical reasons. After the liquid has evaporated, the measurement can be carried out.

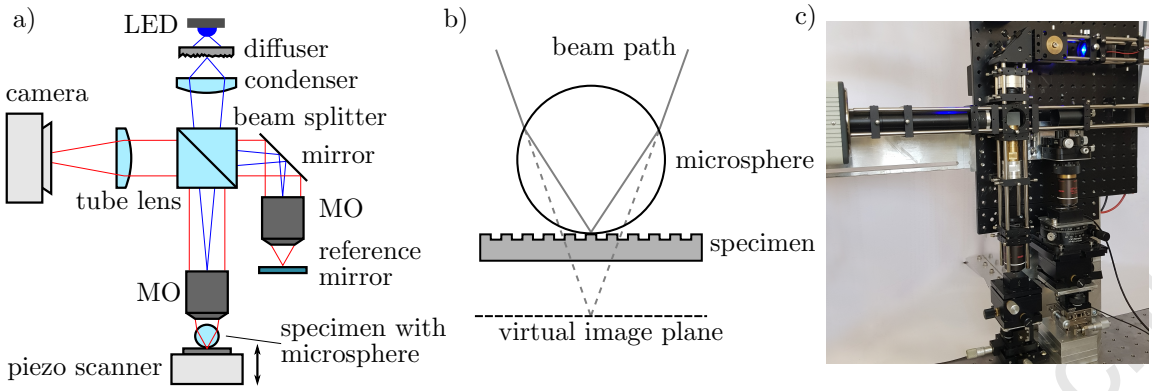

Figure 1. a) Scheme of the Linnik interferometer setup with the microsphere, b) enlarged section showing a specimen with a microsphere on top creating a virtual image plane, c) photograph of the experimental setup in the laboratory.

Throughout this study SiO_2 microspheres with a diameter of 7-10 µm are being used. With the application of microspheres in the imaging path, an axial shift of the focus occurs and creates a virtual image plane as it is sketched in Fig. 1b.

3. ANALYSIS IN THE SPATIAL FREQUENCY DOMAIN

We assume the scattering geometry[34] according to Fig. 2a, where $\mathbf{k}_{\mathrm{in}}$ is the wave vector of a plane wave incident under an angle θ_{in} and $\mathbf{k}_{\mathrm{r}}$ and $\mathbf{k}_{\mathrm{s}}$ are wave vectors of reflected and scattered waves propagating under the angles θ_{r} and θ_{s}, respectively. For a grating with a period Λ_{min} corresponding to the Abbe limit according to (1) the situation is outlined in Fig. 2b. For the incidence angle $\theta_{\mathrm{in}} = \theta_{\mathrm{max}}$ the zeroth order diffracted wave with wave vector $\mathbf{k}_{\mathrm{r}}$ propagates under the angle $\theta_{\mathrm{r}} = \theta_{\mathrm{max}}$, whereas the scattering angle of the minus first order diffracted wave is $\theta_{\mathrm{s}} = -\theta_{\mathrm{max}}$. The scattered electric field $U_{\mathrm{s}}(\mathbf{q})$ under the Fraunhofer far-field condition can be calculated using the Kirchhoff formulation[24,34] with respect to a microscope in reflection mode assuming a perfectly reflecting surface $s(x, y)$ by

$$\begin{aligned} U_{\mathrm{s}}(\mathbf{q}) &= \frac{1}{A}\int_{A} \mathrm{e}^{-\mathrm{i}(q_x x + q_y y + q_z s(x,y))}\,\mathrm{d}x\,\mathrm{d}y \\ &= \frac{1}{A}\int_{-\infty}^{+\infty} A(x,y)\ \mathrm{e}^{-\mathrm{i}(q_x x + q_y y + q_z s(x,y))}\,\mathrm{d}x\,\mathrm{d}y \\ &= \frac{1}{A}\,\mathcal{F}\{A(x,y)\} * \mathcal{F}\{\mathrm{e}^{-\mathrm{i}q_z s(x,y)}\}, \end{aligned} \tag{2}$$

where a monochromatic plane wave of wavelength λ and wavenumber $k_0 = 2\pi/\lambda$ is incident under the angle θ_{in} and the vector $\mathbf{q} = \mathbf{k}_{\mathrm{s}} - \mathbf{k}_{\mathrm{in}}$ defines a point in the 3D Fourier domain. The scattered far-field $U_{\mathrm{s}}(\mathbf{q})$ is normalized in a way that for a smooth surface and perpendicular incidence, i.e. $\theta_{\mathrm{in}} = 0$, the amplitude in the specular direction becomes unity. The area $A(x, y)$ of integration in (2) corresponds to the field of view of the microscope, $\mathcal{F}\{\ldots\}$ represents the Fourier transform, and $*$ the convolution symbol. For a surface textured in one dimension only $s(x, y) = s(x)$ results. If the area A is large enough, (2) represents the two-dimensional Fourier transformation with respect to x and y of the phase object $\exp(-\mathrm{i}q_z s(x, y))$. If, for simplicity $s(x, y) = s(x)$ and considering wave vectors $\mathbf{k}_{\mathrm{in}}$ and $\mathbf{k}_{\mathrm{in}}$ only in the xz-plane, which then equals the plane of incidence and observation, the incident and scattered wave vectors are given by

$$\mathbf{k}_{\mathrm{in}} = k_0 \begin{pmatrix} \sin\theta_{\mathrm{in}} \\ 0 \\ -\cos\theta_{\mathrm{in}} \end{pmatrix} \quad \text{and} \quad \mathbf{k}_{\mathrm{s}} = k_0 \begin{pmatrix} \sin\theta_{\mathrm{s}} \\ 0 \\ \cos\theta_{\mathrm{s}} \end{pmatrix}. \tag{3}$$

Thus, the vector $\mathbf{q}$ results in

$$\mathbf{q} = \begin{pmatrix} q_x \\ q_y \\ q_z \end{pmatrix} = k_0 \begin{pmatrix} \sin\theta_\mathrm{s} - \sin\theta_\mathrm{in} \\ 0 \\ \cos\theta_\mathrm{s} + \cos\theta_\mathrm{in} \end{pmatrix}. \tag{4}$$

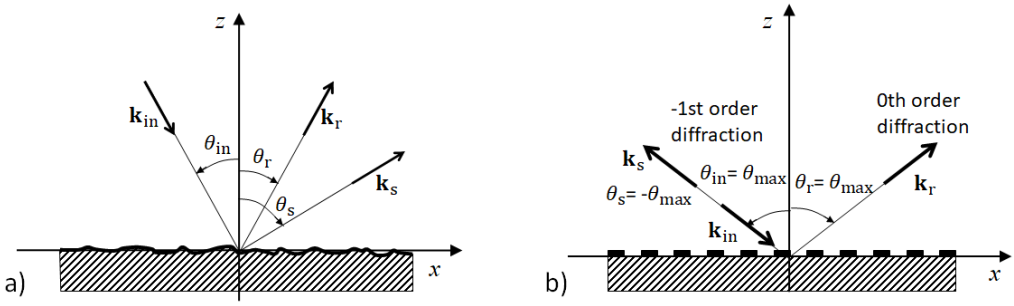

Figure 2. a) Incident, reflected and scattered wave vectors in the xz-plane, b) reflected and -1st order diffracted wave vectors in the xz-plane for a plane wave incident on a grating under the maximum angle θ_max restricted by the numerical aperture of a objective lens.

According to (4), the situation displayed in Fig. 2b leads to

$$|q_x| = 2k_0 \sin\theta_\mathrm{max} = 2k_0\,\mathrm{NA} = \frac{2\pi}{\Lambda_\mathrm{min}}, \tag{5}$$

the maximum lateral spatial frequency collected by a microscope lens of given NA value. (5) is directly related to the Abbe resolution limit according to (1). The coordinates in $\mathbf{q}$-space follow from the Ewald sphere construction shown in Fig. 3. Due to the NA of the microscope, the possible directions of the wave vectors of incident and scattered light are limited by the angle θ_max. According to Fig. 3a, this results in the two spherical caps, which need to be correlated in order to calculate the 3D transfer function $H(\mathbf{q})$ of the instrument.[30] The outer boundary of the resulting Ewald-limiting-sphere is plotted in Fig. 3b, where the contributions of the specular reflection are located on the q_z-axis and the outer spherical shell of radius $2k_0$ represents the back scattered light. Note that the q_x-value represents the spatial frequency component of a surface, whereas the corresponding q_z-values represent the spectral range of the corresponding interference signals. The whole construction shows rotational symmetry with respect to the q_z axis. Fig. 3c displays a 2D cross sectional view in the q_xq_z-plane of $H(\mathbf{q})$, which holds for plane mirror-like surfaces and diffraction gratings.[31] Once $U_\mathrm{s}(\mathbf{q})$ and $H(\mathbf{q})$ are known, the 3D spatial frequency representation of the interference intensity equals the product:

$$\Delta\tilde{I}(\mathbf{q}) = U_\mathrm{s}(\mathbf{q})\; H(\mathbf{q}) \tag{6}$$

and the interference image stack $\Delta I(x,y,z)$ can be calculated via inverse 3D Fourier transform:

$$\Delta I(x,y,z) \sim \mathfrak{Re}\left\{\mathcal{F}^{-1}\left\{\Delta\tilde{I}(\mathbf{q})\right\}\right\}. \tag{7}$$

Cross sections of experimentally obtained spatial frequency representations $\Delta\tilde{I}(\mathbf{q})$ for different rectangular silicon phase gratings (RS-N standard) are depicted in Fig. 4. Figure 4a represents the result for a rectangular grating of 6 µm period and 192 nm peak-to-valley (PV) amplitude, whereas Figs. 4b and c belong to gratings of 400 nm (b) and 300 nm period (c), both with a PV amplitude of 140 nm. The shape of the Ewald-limiting-sphere can be clearly recognized in Fig. 4a. Figures 4b and c show only three diffraction orders, the 0th order at $q_x = 0$ as well as the 1st and -1st orders, which are located at higher q_x valus for the shorter period.

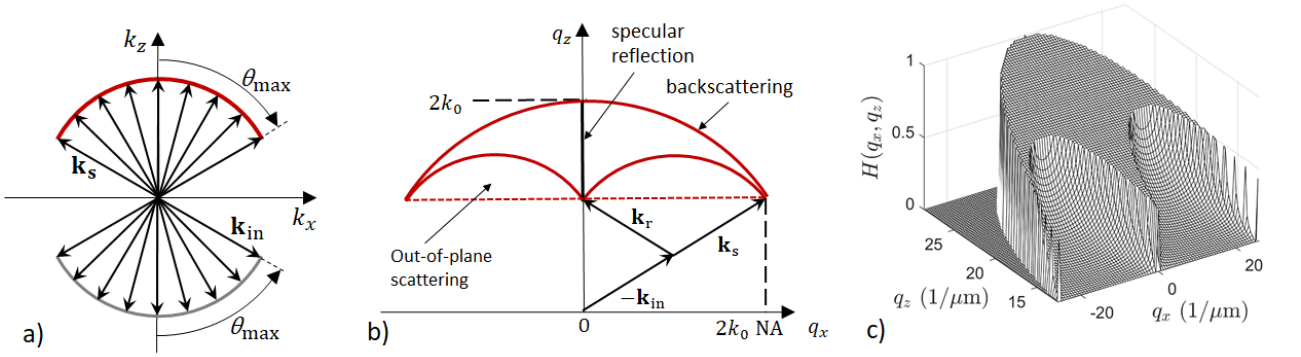

Figure 3. a) Ewald sphere construction based on two spherical caps defined by numerous wave vectors $\mathbf{k}_{\text{in}}$ and $\mathbf{k}_{\text{s}}$ with angles θ_{in} and θ_{s} below the maximum angle θ_{max} corresponding to the NA of the objective lens, b) Ewald-limiting-sphere resulting from the correlation of the two caps, c) 3D transfer function for an interference miccroscope with NA= 0.9 and $\lambda = 440\,\text{nm}$.[31]

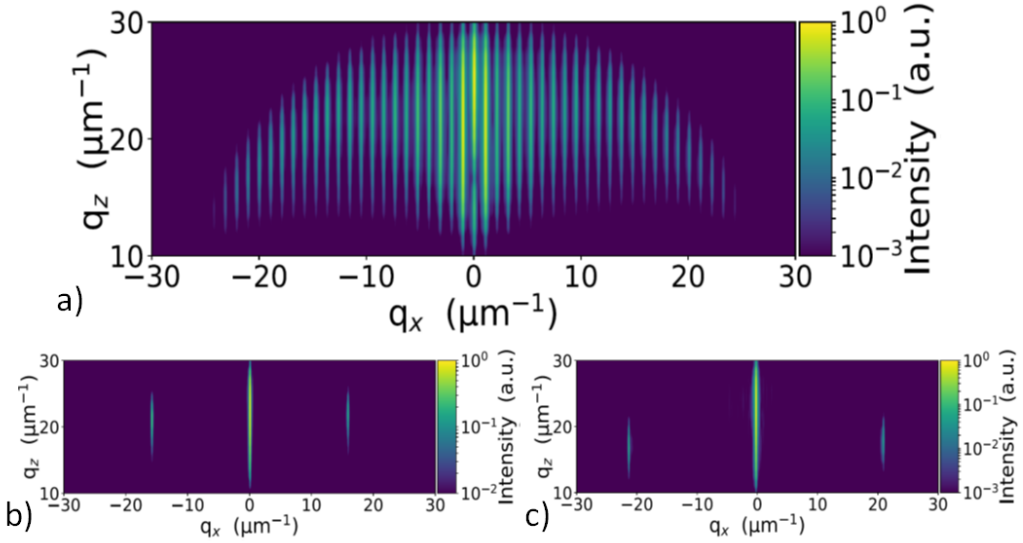

Figure 4. Cross-section of the 3D spatial frequency representation of an interference image stack obtained without a microsphere for, a) a rectangular grating with 6 µm period and 192 nm height difference (RS-N standard by Simetrics), b) a rectangular grating with 0.4 µm period and 140 nm height difference and c) a rectangular grating with 0.3 µm period and 140 nm height difference.

4. RAY-TRACING RESULTS FOR A MICROSPHERE

We already demonstrated that a phase grating with a minimum period length of 230 nm is resolved by the Linnik interferometer mentioned above in combination with microsphere assistance.[35] This period is slightly below the Abbe resolution limit of 244 nm, which holds for this interferometer without a microsphere. This section is intended to study, how light rays are refracted, reflected and focused by the microsphere in order to find out plausible mechanisms for the resolution enhancement. Since we use microspheres of at least 7 µm diameter ($r = 3.5\,\mu\text{m}$), the Mie-parameter $2\pi k_0 r/\lambda$ is at least 50 and a physical description based on geometrical optics is a satisfying approximation to study basic effects.[36] Figure 5 shows some results of ray tracing computations assuming a microsphere of silica with a refractive index of 1.4655. In Fig. 5a a bundle of parallel light rays propagates along the vertical axis and hits the microsphere. The refracted light propagates through the microsphere, is refracted again and shows grazing incidence with respect to a horizontal line located directly under the

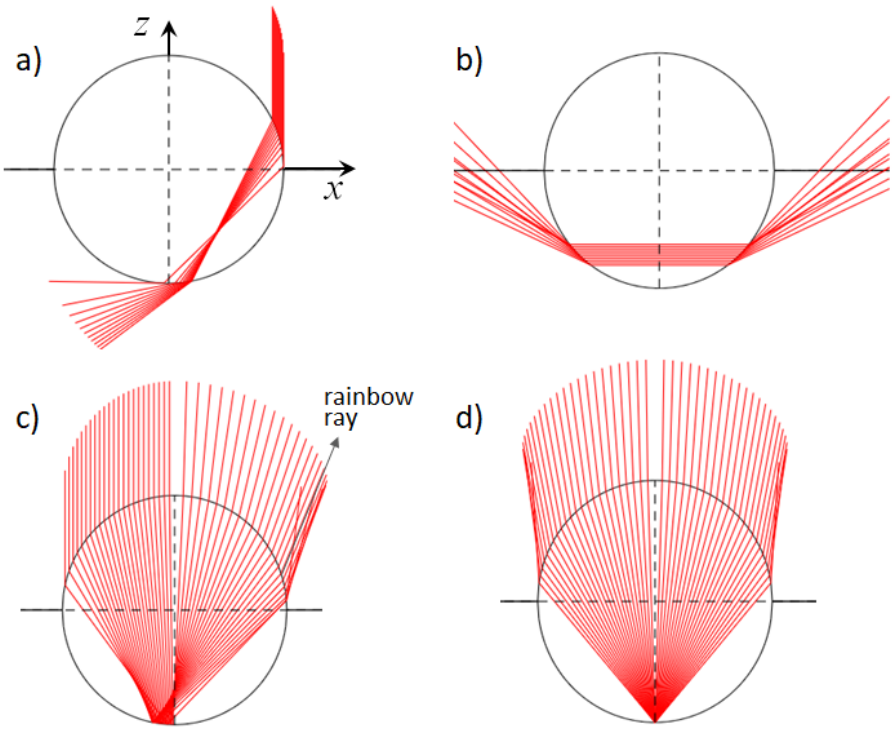

Figure 5. Ray-tracing computations for a silica microsphere of refractive index $n_r = 1.4655$ at $\lambda = 440\,\text{nm}$, a) bundle of rays incident under an angle $\theta_{\text{in}} = 0$, b) rays traveling horizontally through the microsphere, c) internally reflected bundle of rays incident under an angle $\theta_{\text{in}} = 0$, d) incident rays internally reflected at the position $x = 0$, $z = -r$ inside the sphere.

microsphere, where the object is typically placed. Due to the large angle of nearly 90° (defined with respect to the z-axis) of these rays refracted twice, the effective NA of the microsphere as an optical imaging element will be close to unity. There are additional situations shown in Fig. 5b to d, where the light never reaches a measuring object located underneath the microsphere. These ray paths lead to additional interference components although they are not affected by the surface of the measuring object. In Fig. 5b the incident light rays show a relatively large angle of incidence with respect to the z-axis. However, all angles are below the maximum angle θ_{max} defined by the NA of the system. The rays travel horizontally through the microsphere. Due to the symmetry of the arrangement the scattering angle equals the angle of incidence, i.e. $\theta_{\text{s}} = \theta_{\text{in}}$. Hence, for these rays $q_x = 0$ and the corresponding q_z-values are relatively small. In Fig. 5c parallel rays are incident on the left hand side. These rays are refracted at the boundary of the microsphere and are then internally reflected at the bottom of the sphere. After an additional refraction, they propagate in air and include relatively small angles with the z-axis, thus the corresponding q_x-values are low and q_z-values high. This is the arrangement belonging to the rainbow and, indeed, the rainbow ray[36] can be identified as the ray on the right hand side, which corresponds to the maximum scattering angle. The rays close to the rainbow ray form a caustic and thus, in these regions high intensity values occur. A similar situation is illustrated in Fig. 5d, which shows symmetry with respect to the z-axis, since all rays are internally reflected at the coordinate $x = 0$, $z = -r$ inside the microsphere and, therefore, $q_x = 0$ for these rays. Figure 5d demonstrates that the incident and scattered rays again include rather small angles with the z-axes such that no total internal reflection occurs. Light incident at higher angles is no longer reflected at $x = 0$, $z = -r$. Therefore q_z is quite high for the rays plotted in Fig. 5d.

5. EXPERIMENTAL RESULTS

The interferometric measurement data is acquired through a stepwise depth scan with a step height of 20 nm performed by a piezo scanner. This results in a measuring process known from coherence scanning interferometry

(CSI), however, additionally utilizing microsphere assistance. The measurement object is the RS-N resolution standard by Simetrics. Mainly the 300 nm and 600 nm grating structures with nominal depths of 140 nm and 160 nm, respectively, are examined.

While performing CSI measurements, the height information of the specimen's surface is encoded in the phase of the interference signals. To gain a better understanding of the phase modulation occurring in interferometric measurement, xz-cross sections of (offset-free) interference images acquired through a depth scan are depicted in Fig. 6. The results shown in a and b are obtained from the 300 nm and 600 nm grating structure of the RS-N standard using microsphere assistance, i.e. placing a microsphere directly on the grating structure. For comparison, Fig. 6c shows how the image stacks recorded for a mirror instead of a grating leads to highest contrast of the modulation in z-direction of the interference signals centered around the virtual image plane. In x-direction the phase modulation introduced by the surface of the measured grating structures is visible in Fig. 6a and b. The interference signals can be analyzed using envelope- and phase retrieving algorithms in order to reconstruct the grating structure of the object as previously shown.[35] Besides the resolution enhancement through the imaging process, also an additional magnification is introduced by the microspheres.

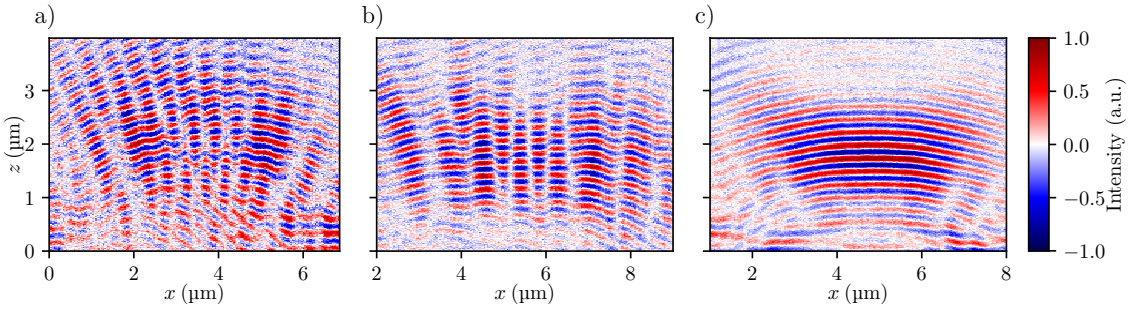

Figure 6. xz-cross sections of offset-reduced interference image stacks acquired with microsphere assistance via a depth scan using royal blue illumination of rectangular silicon gratings (RS-N standard) with period lengths of a) 300 nm, b) 600 nm, and c) a mirror surface for comparison.

For comparability with the results shown in sections 3 and 4 the spatial frequency domain representation of the interference data is analyzed as introduced beforehand. First, the data are preprocessed by means of blackman-windowing as well as zero-padding in order to exclude contributions occurring besides the microsphere and to improve the spatial frequency resolution, respectively. The data are further offset reduced. Cross sections of the spatial frequency representation in the q_xq_z-plane are depicted in Fig. 7 accordingly.

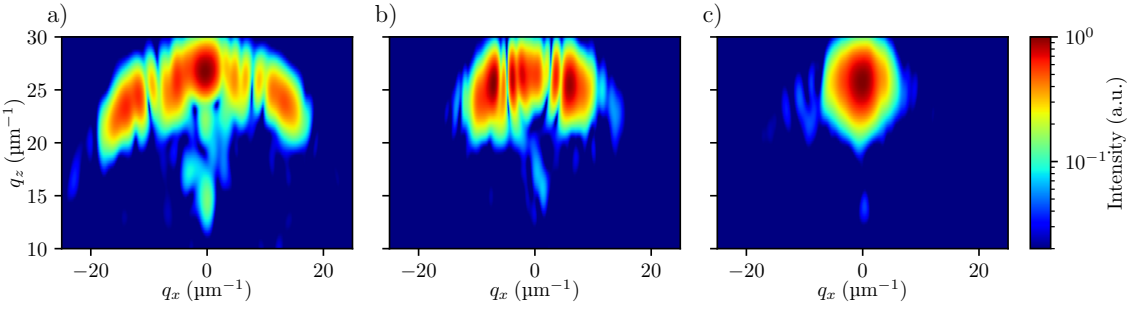

Figure 7. q_xq_z-cross-sections of 3D spatial frequency representations of the interference image stacks corresponding to a) the 300 nm grating structure, b) the 600 nm structure, and c) the mirror surface.

As it is shown in (5) and illustrated in Fig. 4, for a one-dimensional grating structure imaged by an interference

microscope, the diffraction orders are visible as corresponding sharp lines at q_x = const. in the 3D spatial frequency representation. The additional magnification factor introduced by the microsphere was determined to be $M = 1.4$ for our setup. Thus, for the grating of 300 nm period the q_x-value corresponding to the first order diffraction maximum is shifted by the mircosphere from $q_{x,a} \approx \pm 21\,\mu\text{m}^{-1}$ in Fig. 4c to $q_{x,a} \approx \pm 15\,\mu\text{m}^{-1}$ according to Fig. 7a, since the period length Λ is multiplied by M. Consequently, the 600 nm grating magnified by the microsphere leads to first order diffraction maxima at $q_{x,a} \approx \pm 7.5\,\mu\text{m}^{-1}$ as it is displayed in Fig. 7b. Finally, for the mirror no diffraction order except for the zero-order located at $q_x = 0$ appears, as Fig. 7c shows.

Further, the transfer behavior of the microsphere assisted setup differs compared to an interference microscope without a microsphere. The size of the field of view limited by the microsphere significantly influences the intensity distribution in the 3D spatial frequency domain. According to (2), the field of view corresponds to the area of integration described by $A(x, y)$. This leads to a convolution in the 3D spatial frequency domain of the diffraction pattern of the grating with an Airy-disk function (implying a circular shaped field of view). The smaller the field of view $A(x, y)$ the broader is this Airy-disk and the corresponding blurring of the diffraction maxima. Due to optical aberrations introduced by the microsphere and a blackman window used to extract the relevant lateral and axial range in the spatial domain, the frequency response is additionally affected. As a result, a broadening of the discrete intensity pattern, i.e. the sharp lines at certain q_x-values initiated by diffraction at the grating structure, occurs. This becomes apparent by comparison of Fig. 7a, b and Fig. 4. Besides the light diffracted by the grating, additional intensity contributions in Fig. 7 can be attributed to the microsphere itself, e.g. the intensity maximum at $q_x = 0$, $q_z \approx \pm 15\,\mu\text{m}^{-1}$, which corresponds to the situation according to Fig. 5b and the higher frequency rippling, which is a consequence of the increased scattered light intensity under the rainbow angle shown in Fig. 5c.

6. RIGOROUS SIMULATIONS

The measured data is compared to simulation results of the imaging process, where the light-surface interaction considering the microsphere is based on rigorous FEM (finite element method) computation of the electric field distribution. The transfer characteristics of the interference microscope as well as the phase shifts introduced by the depth scan are considered by filter operations using Fourier optics modeling. The combined model enables a full 3D simulation of illumination and diffraction at 2D periodic surfaces and provides accurate results compared with CSI measurements.[37,38] In this study, the model is extended considering a microsphere with a radius of $r = 2.5\,\mu\text{m}$ and a refractive index of $n = 1.5$, which is placed directly on the specimen. For computational reasons microspheres a arranged in a periodic manner with a period length $L_x = 13.2\,\mu\text{m}$. Due to computational and time constraints, the simulation is performed on 2D surface structures and hence, the microsphere is approximated by a microcylinder. However, using spider silk also cylindrical microelements were shown to enhance the resolution.[39] Since we are interested in general effects of microsphere induced resolution enhancement, it is reasonable not to use exactly the same configuration for measurement and simulation.

Figure 8 shows extracts of offset reduced interference image stacks in the presence of a microsphere simulated with TM polarized monochromatic light of $\lambda = 440\,\text{nm}$ and NA= 0.9. Due to the high NA value, the light source can be assumed as monochromatic, since the influence of temporal coherence is negligible for single colored LEDs. The underlying structure is a sinusoidal grating with PV height of 25 nm and period lengths corresponding to those of the measured results displayed in Fig. 6. In order to avoid additional effects such as multiple scattering and edge diffraction, the height is chosen to be smaller compared to the measured profile.

Comparing Figs. 6 and 8, qualitative agreement between measured and simulated data stacks is obtained. In both figures, the grating structure appears in the phase of the interference signals. Similar to the measurement result, the simulated interference signals obtained from a flat mirror (Fig. 8c) do not show a grating dependent phase modulation. Detailed comparison of simulated and measured results exhibits deviations. These are mainly due to the fact that results measured using a sphere are compared to simulation results obtained from a cylinder. Further, the sphere is arbitrarily placed on the grating and thus at different positions with respect to the grating structure in simulations. Additionally, the spheres have a different radius compared to the cylinder leading to further deviations.

More quantitative comparisons will be published in future.

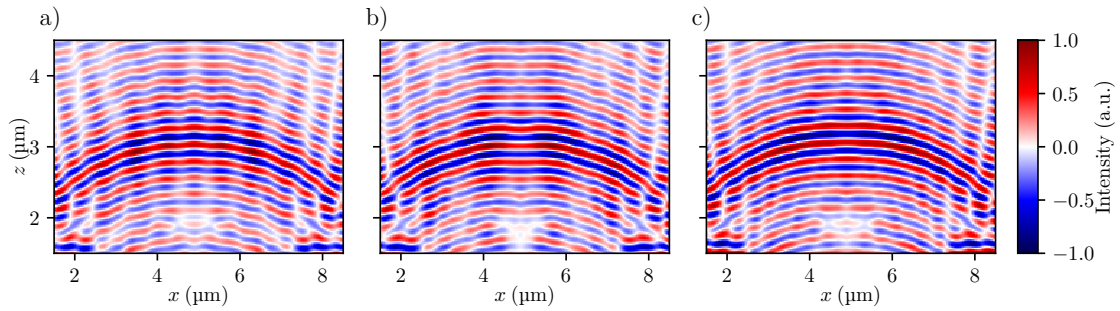

Figure 8. xz-cross sections of offset-reduced interference image stacks obtained by rigorous simulation.[38] The periods of the underlying sinusoidal grating structure of 25 nm PV amplitude correspond to the RS-N resolution standard with period length of a) 300 nm, and b) 600 nm, c) results of a flat mirror surface for comparison.

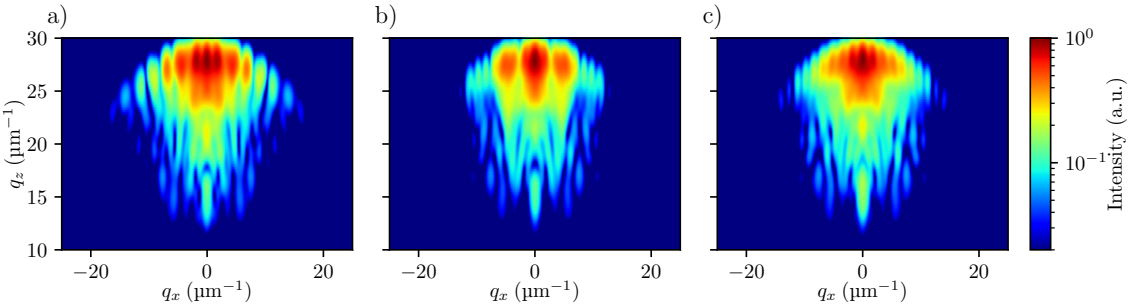

Figure 9. q_xq_z-cross-sections of 3D spatial frequency representations of the simulated interference image stacks corresponding to a) the 300 nm sinusoidal grating, b) the 600 nm grating, and c) the mirror surface.

In order to analyze the interference signals in more detail, Fig. 9 shows the representation in **q**-space. Comparing simulation and measurement results, the diffraction orders are blurred in the measurement results. The intensity obtained from a plane mirror (Fig. 9c) shows an additional periodic modulation of the intensity distribution for larger q_z and small q_x values. This is probably a consequence of the rainbow effect explained in Ch. 4, since simulations turn out that the modulation period behaves antiproportional to the microsphere's diameter. This phenomenon is not as clearly observed in the measurement results obtained from a plane mirror, but the differences can be explained by the use of microcylinders in the simulation instead of spheres.

However, a slight modulation can be observed even in the measurement results, especially in case of Figs. 7a and 7b. Furthermore, in both, measurement and simulation, an intensity contribution at $q_x = 0$ for small values of q_z is visible with and without a grating structure. This can be assigned to the rays travelling horizontally through the microsphere as it is demonstrated in Fig. 5b and confirmed by simulations assuming a microsphere in free space. The high intensity for large q_z values and $q_x \approx 0$ follow from the rays depicted in Fig. 5d, where rays of oblique incidence and scattering angles inside the sphere are refracted such that above the sphere smaller angles and hence larger values of q_z result.

In sum, the rigorous simulation model reproduces the major effects occurring in measurement results. Artefacts observed in the 3D spatial frequency domain can be assigned to general cases of ray tracing. Thus, the **q**-space representation is shown to be quite useful in order to analyze the physical mechanism introduced by microspheres. Furthermore, diffraction orders belonging to the measured grating structure under the sphere lead to smaller q_x and larger q_z values due to the magnification of the sphere as supposed by Hüser and Lehmann.[23,35] This effect is now confirmed by simulations of grating structures of different period.

Further simulation studies exhibit an enhanced lateral resolution of nearly 200 nm due to the microsphere

assistance. This corresponds to the lateral resolution according to the Sparrow criterion for an effective NA of 1.0 and is nearly independent of the given NA of the objective lenses. No further enhancement of the lateral resolution could be observed in the presence of whispering gallery modes. The corresponding simulation results will published in future, too.

7. CONCLUSION

Although mircosphere assisted resolution enhancement is frequently used in optical imaging and 3D microscopy, the physical mechanism behind this phenomenon is still not completely understood. The most frequently mentioned explanation attempts refer to the enhancement of the numerical aperture, the collection of evanescent waves, the photonic nanojet effect, and the excitation of whispering gallery modes.

In order to analyze the resolution enhancement, we compare both, experimental and simulated interference image stacks in the three-dimensional spatial frequency domain. This methodology provides advantages as it explains the occurring phenomena based on light rays travelling under different angles with respect to the optical axis and thus enables comparisons with ray-tracing computations and rigorous simulations as well. In 3D Fourier space effects occurring through the microsphere itself independently of the specimen can be separated from effects introduced by the interaction of the microsphere and the specimen. Microspheres shift the intensity diffraction maxima of a grating to lower spatial frequencies and thus enlarge the magnification of the optical imaging system. In addition, the effective wavelength of the resulting interference signals is significantly reduced if microspheres are used. In combination with ray-tracing and rigorous simulation results we conclude that the effect, which arises from the microspheres, can be viewed as an effective enlargement of the numerical aperture of the optical system.

Since we use 3D microscopy in reflection mode, we suppose direct reflection and diffraction of propagating waves to be dominant and thus implications of evanescent waves to be negligible. We can also exclude whispering gallery modes by comparing simulation results obtained for two slightly different wavelengths. Although only for one wavelength a whispering gallery mode occurs, both results show the same resolution enhancement. Therefore, our investigation suggests that the most likely mechanism is the enhancement of the numerical aperture, which is close to 1.0 in case of microsphere assistance. For our microscope with an NA of 0.9 a resolution enhancement of 11 % is achieved by using microspheres. Since the occurrence of photonic nanojets also relies on the coherent superposition of waves propagating under angles of nearly 90° with respect to optical axis the physical origins of nanojets and NA enhancement are closely related to each other. However, the specimen is placed at the location, where the nanojet occurs if the specimen would be left. Hence, the generation of a nanojet will be disturbed and an interaction of the corresponding electromagnetic waves with the specimen takes place.

ACKNOWLEDGMENTS

The partial support of this project by the DFG (German Research Foundation) under grant number LE992/15-1 is gratefully acknowledged.

REFERENCES

[1] Wang, Z., Guo, W., Li, L., Luk, B., Khan, A., and Liu, Z., "Supplementary Information Optical virtual imaging at 50 nm lateral resolution with a white light nanoscope," *Nature communications* **2**, 1–7 (2011).

[2] Darafsheh, A., Walsh, G. F., Dal Negro, L., and Astratov, V. N., "Optical super-resolution by high-index liquid-immersed microspheres," *Applied Physics Letters* **101**(14), 141128 (2012).

[3] Darafsheh, A., Limberopoulos, N. I., Derov, J. S., Walker, D. E., and Astratov, V. N., "Advantages of microsphere-assisted super-resolution imaging technique over solid immersion lens and confocal microscopies," *Applied Physics Letters* **104**(6) (2014).

[4] Yan, Y., Li, L., Feng, C., Guo, W., Lee, S., and Hong, M., "Microsphere-Coupled Scanning Laser Confocal Nanoscope for Sub-Diffraction-Limited Imaging at 25 nm Lateral Resolution in the Visible Spectrum," *ACS Nano* **8**, 1809–1816 (feb 2014).

[5] Perrin, S., Li, H., Leong-Hoi, A., Lecler, S., and Montgomery, P., "Illumination conditions in microsphere-assisted microscopy," *Journal of Microscopy* **274**(1), 69–75 (2019).

[6] Perrin, S., Li, H., Badu, K., Comparon, T., Quaranta, G., Messaddeq, N., Lemercier, N., Montgomery, P., Vonesch, J. L., and Lecler, S., "Transmission Microsphere-Assisted Dark-Field Microscopy," *Physica Status Solidi - Rapid Research Letters* **13**(2), 1–4 (2019).

[7] Wang, F., Liu, L., Yu, P., Liu, Z., Yu, H., Wang, Y., and Li, W. J., "Three-dimensional super-resolution morphology by near-field assisted white-light interferometry," *Scientific Reports* **6**(April), 24703 (2016).

[8] Perrin, S., Leong-Hoï, A., Lecler, S., Pfeiffer, P., Kassamakov, I., Nolvi, A., Hæggström, E., and Montgomery, P., "Microsphere-assisted phase-shifting profilometry," *Applied Optics* **56**(25), 7249–7255 (2017).

[9] Leong-Hoi, A., Hairaye, C., Perrin, S., Lecler, S., Pfeiffer, P., and Montgomery, P., "High Resolution Microsphere-Assisted Interference Microscopy for 3D Characterization of Nanomaterials," *Physica Status Solidi (A) Applications and Materials Science* **215**(6), 1–7 (2018).

[10] Montgomery, P. C., Lecler, S., Leong-hoï, A., Perrin, S., and Pfeiffer, P., "Sub-diffraction surface topography measurement using a microsphere- assisted Linnik interferometer," *Proceedings of SPIE - The International Society for Optical Engineering* **10329**(33), 1–10 (2017).

[11] Montgomery, P., Lecler, S., Leong-Hoi, A., and Pfeiffer, P., "3D nano surface profilometry by combining the photonic nanojet with interferometry," *Journal of Physics: Conf. Series* **794**(1), 012006 (2017).

[12] Kassamakov, I., Lecler, S., Nolvi, A., Leong-Hoï, A., Montgomery, P., and Hæggström, E., "3D Super-Resolution Optical Profiling Using Microsphere Enhanced Mirau Interferometry," *Scientific Reports* **7**(1), 1–7 (2017).

[13] Yang, H., Trouillon, R., Huszka, G., and Gijs, M. A., "Super-Resolution Imaging of a Dielectric Microsphere Is Governed by the Waist of Its Photonic Nanojet," *Nano Letters* **16**(8), 4862–4870 (2016).

[14] Maslov, A. and Astratov, V., "Resolution and Reciprocity in Microspherical Nanoscopy: Point-Spread Function Versus Photonic Nanojets," *Physical Review Applied* **11**(6), 064004 (2019).

[15] Luk'yanchuk, B. S., Paniagua-Domínguez, R., Minin, I., Minin, O., and Wang, Z., "Refractive index less than two: photonic nanojets yesterday, today and tomorrow [Invited]," *Optical Materials Express* **7**(6), 1820 (2017).

[16] Heifertz, A., Kong, S.-C., Sahakian, A. V., Taflove, A., and Backman, V., "Photonic Nanojets," *Comput Theor Nanosci.* **6**(9), 1979–1992 (2009).

[17] Rockstuhl, C., Kim, M.-S., Herzig, H. P., Scharf, T., and Mühlig, S., "Engineering photonic nanojets," *Optics Express* **19**(11), 10206 (2011).

[18] Kim, M. S., Scharf, T., Mühlig, S., Rockstuhl, C., and Herzig, H. P., "Gouy phase anomaly in photonic nanojets," *Applied Physics Letters* **98**(19), 2–5 (2011).

[19] Zhou, S., Deng, Y., Zhou, W., Yu, M., Urbach, H. P., and Wu, Y., "Effects of whispering gallery mode in microsphere super-resolution imaging," *Applied Physics B: Lasers and Optics* **123**(9), 1–9 (2017).

[20] Ben-Aryeh, Y., "Increase of resolution by use of microspheres related to complex Snell's law," *Journal of the Optical Society of America A* **33**(12), 2284 (2016).

[21] Darafsheh, A., "Microsphere-assisted microscopy," *Journal of Applied Physics* **131**(3), 031102 (2022).

[22] Wu, M. X., Huang, B. J., Chen, R., Yang, Y., Wu, J. F., Ji, R., Chen, X. D., and Hong, M. H., "Modulation of photonic nanojets generated by microspheres decorated with concentric rings," *Optics Express* **23**(15), 20096 (2015).

[23] Hüser, L. and Lehmann, P., "Analysis of resolution enhancement through microsphere-assisted interferometry in the 3D spatial frequency domain," in [*Proceedings of SPIE - The International Society for Optical Engineering*], (June), 25 (2021).

[24] Sheppard, C. J., Connolly, T. J., and Gu, M., "Imaging and reconstruction for rough surface scattering in the kirchhoff approximation by confocal microscopy," *Journal of Modern Optics* **40**(12), 2407–2421 (1993).

[25] Quartel, J. C. and Sheppard, C. J., "A surface reconstruction algorithm based on confocal interferometric profiling," *Journal of Modern Optics* **43**(3), 591–605 (1996).

[26] Quartel, J. C. and Sheppard, C. J., "Surface reconstruction using an algorithm based on confocal imaging," *Journal of Modern Optics* **43**(3), 469–486 (1996).

[27] Coupland, J., Mandal, R., Palodhi, K., and Leach, R., "Coherence scanning interferometry: Linear theory of surface measurement," *Applied Optics* **52**(16), 3662–3670 (2013).

[28] Su, R., Coupland, J., Sheppard, C., and Leach, R., "Scattering and three-dimensional imaging in surface topography measuring interference microscopy," *Journal of the Optical Society of America A* **38**(2), A27 (2021).
[29] Lehmann, P., Künne, M., and Pahl, T., "Analysis of interference microscopy in the spatial frequency domain," *Journal of Physics: Photonics* **3**(014006), 1–17 (2021).
[30] Lehmann, P. and Pahl, T., "Three-dimensional transfer function of optical microscopes in reflection mode," *Journal of Microscopy* **284**, 45–55 (oct 2021).
[31] Lehmann, P., Hagemeier, S., and Pahl, T., "Three-Dimensional Transfer Functions of Interference Microscopes," *Metrology* **1**(2), 122–141 (2021).
[32] Hüser, L. and Lehmann, P., "Microsphere-assisted interference microscopy for resolution enhancement," *Technisches Messen* **88**(5), 311–318 (2021).
[33] Tereschenko, S., *Digitale Analyse periodischer und transienter Messsignale anhand von Beispielen aus der optischen Präzisionsmesstechnik*, PhD thesis, Universität Kassel (2018).
[34] Beckmann, P. and Spizzichino, A., "The scattering of electromagnetic waves from rough surfaces," *Norwood: Artech House Inc.* (1987).
[35] Hüser, L. and Lehmann, P., "Microsphere assisted interferometry with high numerical apertures for 3D topography measurements," *Applied Optics* **59**(6), 1695–1702 (2020).
[36] van de Hulst, H. C., [*Light scattering by small particles*], Dover Publications, Inc (1981).
[37] Pahl, T., Hagemeier, S., Hüser, L., Xie, W., and Lehmann, P., "Two-dimensional modelling of systematic surface height deviations in optical interference microscopy based on rigorous near field calculation," *Journal of Modern Optics* **67**(11), 963–973 (2020).
[38] Pahl, T., Hagemeier, S., Künne, M., Yang, D., and Lehmann, P., "3D modeling of coherence scanning interferometry on 2D surfaces using FEM," *Optics Express* **28**(26), 39807 (2020).
[39] Monks, J. N., Yan, B., Hawkins, N., Vollrath, F., and Wang, Z., "Spider Silk: Mother Nature's Bio-Superlens," *Nano Letters* **16**(9), 5842–5845 (2016).

L. Hüser, T. Pahl, M. Künne, P. Lehmann, "The use of microsphere assistance in interference microscopy with high numerical aperture objective lenses" SPIE Proceedings 12152, Mesophotonics: Physics and Systems at Mesoscale, 1215204, (May 24, 2022).

https://doi.org/10.1117/12.2622892